

Wedge transducer design for two-dimensional ultrasonic manipulation in a microfluidic chip

O Manneberg, J Svennebring, H M Hertz and M Wiklund

Biomedical & X-Ray Physics, Department of Applied Physics, Royal Institute of Technology, KTH/AlbaNova, SE-10691 Stockholm, Sweden

Received 21 May 2008, in final form 22 July 2008

Published 14 August 2008

Online at stacks.iop.org/JMM/18/095025

Abstract

We analyze and optimize the design of wedge transducers used for the excitation of resonances in the channel of a microfluidic chip in order to efficiently manipulate particles or cells in more than one dimension. The design procedure is based on (1) theoretical modeling of acoustic resonances in the transducer–chip system and calculation of the force fields in the fluid channel, (2) full-system resonance characterization by impedance spectroscopy and (3) image analysis of the particle distribution after ultrasonic manipulation. We optimize the transducer design in terms of actuation frequency, wedge angle and placement on top of the chip, and we characterize and compare the coupling effects in orthogonal directions between single- and dual-frequency ultrasonic actuation. The design results are verified by demonstrating arraying and alignment of particles in two dimensions. Since the device is compatible with high-resolution optical microscopy, the target application is dynamic cell characterization combined with improved microfluidic sample transport.

1. Introduction

Ultrasonic particle manipulation in microfluidic chips is an emerging tool in lab-on-a-chip systems with applications such as washing [1, 2], separation [3, 4], positioning [5], aggregation [6, 7] and assaying [8, 9] of bio-functionalized particles or cells. Most of the previously reported micro-machined systems employ single-frequency, near-one-dimensional (1D) ultrasonic fields for focusing particles into vertically oriented pressure node planes of the standing wave [5, 10, 11]. However, a less desired effect with this arrangement is that the particles settle to the lower surface of the microchannel due to gravity [10, 12]. In pressure-driven flows with near-parabolic flow profiles, the result is a large variation in particle speeds and a significantly increased risk of adhesion of particles or cells to the channel surfaces that may cause problems such as sample loss, sample contamination and channel clogging. In order to solve this problem, we have previously demonstrated preliminary results on two-dimensional (2D) continuous alignment of particles based on combining (horizontal) focusing and (vertical) levitation of particles in a microfluidic chip [13]. In the present paper, we provide a detailed analysis and design optimization of our

wedge-transducer-based actuation method, and verification of this design by demonstration of both arraying and alignment in 2D of micro-particles or cells in microfluidic chips.

Different strategies have been suggested for achieving 2D ultrasonic resonances in microfluidic chips. These include transducer-based methods [9, 14], channel-geometry-based methods [15, 16] or a combination of both [17]. However, all these devices operate on a single frequency [9, 14–16] or on two near-identical frequencies [17]. Therefore, the orthogonal components of the generated 2D field are strongly coupled and the result is an unpredictable and/or complicated pattern of the manipulated particles.

We have previously demonstrated ultrasonic manipulation in microfluidic chips based on oblique coupling of ultrasound from external transducers combined with refractive wedges [10, 18, 19]. Important advantages of this coupling method are compatibility with high-resolution optical microscopy, and the flexibility and small size of the transducers. Furthermore, we have demonstrated multi-frequency operation by use of several wedge transducers simultaneously [13, 19]. To a first approximation, one could believe that the direction of the incident wave into the fluid channel can be derived by simply using Snell's law of wave refraction on a plane incident wave in

the wedge. However, this simplified model is not applicable to a transducer-microfluidic chip system where most of its dimensions are comparable to the acoustic wavelength. Thus, in order to optimize the coupling and control the properties of the generated acoustic field in the channel, it is necessary to analyze the full transducer–chip system.

In the present paper, we investigate and optimize the design of wedge transducers for 2D ultrasonic manipulation of particles or cells in a microfluidic chip. The coupling mechanism and the corresponding force field in the channel are investigated with (1) theoretical modeling of the acoustic field and (2) impedance measurements of the transducer–chip system, and with (3) image analysis of the particle distribution after ultrasonic actuation. In particular, we investigate the dependence of the wedge angle on the manipulation performance, as well as to what extent it is possible to achieve independent 1D standing-wave fields in orthogonal directions inside the channel of a microfluidic chip by remote actuation from external wedge transducers. Finally, we verify our design by demonstrating 2D centering and alignment as well as 2D micro-aggregation and arraying of particles. In the future, our aim is to use the device in cell and bead assays for gentle cell characterization and/or medical diagnosis.

2. Theoretical background

2.1. The ultrasonic radiation force

The theory of ultrasonic radiation forces is well understood [20]. Suspended particles in an ultrasonic standing wave are subjected to a primary radiation force \mathbf{F}_{PR} , which attracts them to the nodes or antinodes of the standing wave depending on the acoustic properties of the particles relative to the surrounding medium [21]. Gor'kov has shown that the force on a particle of volume V in an acoustic field not similar to a plane wave is given by

$$\mathbf{F}_{\text{PR}} = -V \nabla \left(f_1 \frac{\langle p^2 \rangle}{2\rho c} - \frac{3}{2} \rho f_2 \frac{\langle v^2 \rangle}{2} \right), \quad (1)$$

where the brackets denote time-averaging, p is the acoustic pressure, v is the acoustic particle velocity and ρ and c are the density and speed of sound in the medium. f_1 and f_2 are contrast factors which depend on the speed of sound and the density of the medium and particle according to

$$f_1 = 1 - \frac{\rho c^2}{\rho_p c_p^2} \quad \text{and} \quad f_2 = 2 \frac{(\rho_p - \rho)}{2\rho_p + \rho}, \quad (2)$$

where the index 'p' indicates 'particle'.

Within the applicability range of equation (1) [20], we are in particular interested in resonant (stationary) acoustic fields. This gives us the possibility of separating the time and space dependence of the field and rewriting the force \mathbf{F}_{PR} as a function of known parameters and the pressure field only. In this way, we may perform numerical calculations of force fields from simulated pressure fields (cf section 2.2).

We begin by assuming a velocity potential such that $\mathbf{v}(\mathbf{r}, t) = \nabla \Phi(\mathbf{r}, t)$, where \mathbf{r} is the position vector and t the time, for the acoustic field which factors according to

$\Phi(\mathbf{r}, t) = \varphi(\mathbf{r}) \cos(\omega t)$, where ω is the angular frequency. This yields pressure and velocity fields

$$\begin{aligned} P(\mathbf{r}, t) &= -\rho \frac{\partial}{\partial t} \Phi(\mathbf{r}, t) = \underbrace{-\rho \omega \varphi(\mathbf{r})}_{p(\mathbf{r})} (-\sin(\omega t)) \\ \mathbf{v}(\mathbf{r}, t) &= \nabla \Phi = -\nabla \frac{1}{\rho} \int P(\mathbf{r}, t) dt \\ &= -\frac{1}{\rho} \nabla p(\mathbf{r}) \int -\sin(\omega t) dt = -\frac{1}{\rho} \frac{\cos(\omega t)}{\omega} \nabla p(\mathbf{r}). \end{aligned} \quad (3)$$

Substituting these expressions into equation (1) and carrying out the time-averaging now yields

$$\begin{aligned} \mathbf{F}_{\text{PR}} &= -V \left[\frac{f_1}{2\rho c^2} \nabla \left(\frac{1}{2} p^2(\mathbf{r}) \right) \right. \\ &\quad \left. - \frac{3}{4} \rho f_2 \nabla \left(\frac{1}{2\rho^2 \omega^2} (\nabla p(\mathbf{r}))^2 \right) \right], \end{aligned} \quad (4)$$

which, after some algebraic manipulation, can be written as

$$\mathbf{F}_{\text{PR}} = -\frac{V\beta}{2} \left[f_1 p \nabla p - \frac{3f_2}{2k^2} (\nabla p \cdot \nabla) \nabla p \right], \quad (5)$$

where β is the compressibility and $k = \omega/c$ is the wave number, both in the medium.

Finally, it should be mentioned that when several particles are present, each particle will also be subjected to a secondary radiation force, known as the secondary Bjerknes force, which is due to the field scattered from other nearby particles [22]. This attractive secondary force contributes to the formation of closely packed aggregates of particles in the pressure nodes.

2.2. Numerical modeling and calculations

Numerical modeling of the acoustic field in the chip was carried out using the FEM software Comsol Multiphysics [23]. Postprocessing of the calculated pressure field in the microchannel into the primary radiation force field (cf equation (5)) was carried out in MATLAB [24]. All pressure field simulations were performed in 2D cross-sections of the system, as a full 3D-model of the transducer–chip-channel system would demand enormous amounts of computer power. The modeled cross-section planes are marked in figure 1(d) by the dotted line (xy plane), the dashed line (yz plane) and the plane of the paper (zx plane in the middle of the silicon layer). The outer boundaries of the solid structures of the transducer–chip system were set to be free (without any load). Mesh element limits were first set to be the smallest of either $\frac{\lambda}{5}$ or the criterion that a layer should contain at least five mesh points in its 'thin' direction. The mesh was then refined to the limits of the available computer power. The simulations do not take into account scattered pressure fields in the channel, and thus only the primary radiation force is simulated. Neither is streaming or heating effects included, since they are of minor importance in our system and for the particle sizes used [15, 18].

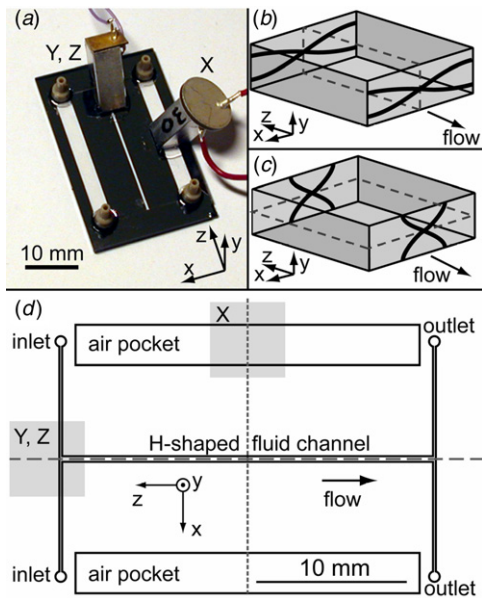


Figure 1. Photograph of the transducer–chip system (a) and schematics of a standing wave along the x -axis (b) and y -axis (c). Pressure nodal planes in (b) and (c) are indicated by the dashed lines; (d) shows a top-view schematic of the silicon layer of the chip, with transducer positions from (a) shown as gray squares. The dashed and dotted lines in (d) are cross-sections discussed in section 4.1.1. (This figure is in colour only in the electronic version)

3. Device

Figure 1 shows a photograph (a) of the transducer–chip system and schematics (b)–(c) demonstrating the idea of two-dimensional (2D) manipulation by orthogonal standing-wave fields. The detailed geometry of the silicon structure is shown in figure 1(d). The H-shaped fluid channel is chosen for flexibility reasons, but the multiple inlets and outlets are not of importance for the work presented in this paper. Each field is generated by a transducer resonantly tuned to a channel dimension. As illustrated in figures 1(b)–(c), the channel dimensions and operating transducer frequencies are matched to fulfill the simplified resonance condition $L = m\lambda/2$, where L is the extent of the channel in the relevant direction, m is a positive integer and λ is the acoustic wavelength in the fluid. This simple design criterion was used in the manufacturing process of the chip, and for selecting the nominal resonance frequencies of the transducers. Air pockets were included in the chip design for defining air-backed quarter-wavelength silicon reflectors in the x -direction.

The chip is made of a $22 \times 34 \text{ mm}^2$ glass–silicon–glass stack with layer thicknesses 0.20 mm, 0.11 mm and 1.0 mm, respectively (GeSim, Germany). A $375 \times 110 \mu\text{m}^2$ (cross-sectional width \times height) channel was etched through the whole silicon layer, creating a fully transparent chip. Ultrasound was coupled into the fluid channel by one or two wedge transducers attached on top of the chip (cf figure 1(a)) by a quick-drying and water-soluble adhesive gel (‘Tensive’, Parker Laboratories, USA). The transducers were made of PZT (lead zirconate titanate) piezoceramic plates (Pz-26, Ferroperm, Denmark) with nominal fundamental thickness

resonances of 6.89, 2.04 and 4.12 MHz, respectively, which were glued to ($5 \times 5 \text{ mm}^2$ cross-section) aluminum wedges with angles of incidence (between the chip surface and the piezoceramic plate) ranging from $\theta_i = 0^\circ$ to $\theta_i = 50^\circ$. The transducers were labeled X, Y and Z, indicating the primary direction (x , y and z , respectively) of the resonance. Efforts were made to make the device fully compatible with any kind of high-resolution optical microscopy, including both epi-fluorescence and trans-illumination techniques. Here, important properties are the coverslip-thickness bottom glass layer, full optical transparency both above and below the channel, and the transducer placement close to the chip edges allowing trans-illumination condenser light (cf figure 1(a)).

Three kinds of beads were employed in the experiments: $10.4 \mu\text{m}$ green-fluorescent polystyrene beads (Bangs Labs, USA), $5 \mu\text{m}$ non-fluorescent polyamide beads (Orgasol, Danish Phantom Design, Denmark) and $1.8 \mu\text{m}$ red-fluorescent polystyrene beads (Polysciences Inc., USA). The $10.4 \mu\text{m}$ beads were chosen for their resemblance to cells in both volume and acoustic properties. The beads were diluted in phosphate-buffered saline (PBS), pH 7.4, with 0.01% Tween-20 and introduced into the chip by use of a syringe pump and Teflon (FEP) tubing.

The mechanism and efficiency of coupling ultrasound via a wedge into the fluid channel were investigated by different methods. Besides the theoretical modeling (cf section 2.2), the coupling was experimentally analyzed by impedance spectroscopy, and the manipulation performance in the channel was characterized by image analysis of sonicated beads. For the impedance spectroscopy, the resonances of the free transducers, and of the transducer–chip assembly with and without a fluid-filled channel, were characterized by an impedance analyzer (Z-check 16777k, Sonosep Technologies, Austria). The analyzer scanned the frequency from 1.8 MHz to 2.1 MHz in steps of 10 kHz on transducers with wedge angles between 0° and 50° (in steps of 10°). The image analysis procedure is described in detail in section 4.1.3.

4. Results and discussion

4.1. Wedge transducer design

4.1.1. Modeling results. Figure 2 shows selected results of modeling the ultrasound field in a transducer–chip system according to the procedure described in section 2.2. The coordinate system is chosen so that the z -axis points in the channel direction (cf figure 1(a)). Figure 2(a) depicts the resulting displacement amplitude in an xy cross-section (vertical plane across the channel, illustrated by a dotted gray line in figure 1(d)) of the transducer and chip when the top surface of the aluminum wedge (where the PZT element is attached; cf section 3) is forced to vibrate at 1.97 MHz. This models the actuation of the X transducer in figures 1(a) and (d), used for creating a standing wave similar to the illustration in figure 1(b). The simulation also yields the pressure field in the channel, which is used for the calculation of the force field according to equation (5). The blow-up inset in figure 2(a) shows the x (upper diagram) and y (lower

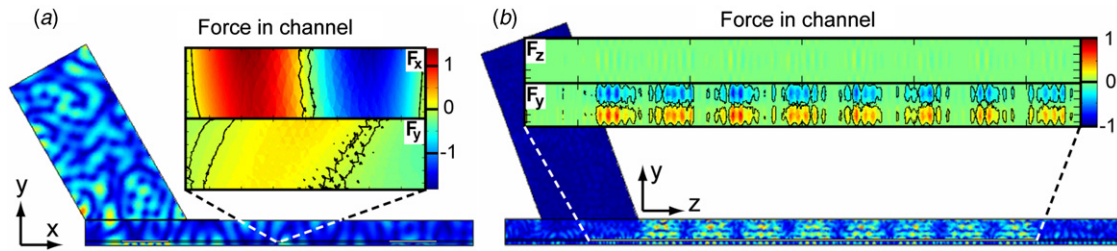


Figure 2. Modeling of acoustic fields in the transducer–chip system in two vertical planes: xy (a) and yz (b) planes. These planes correspond to the dotted and dashed gray lines in figure 1(d), respectively. Figure 2(a) shows the normalized displacement amplitude in an xy cross-section (across the channel) when the source is actuated at 1.97 MHz. The blow-up insets show the x (upper diagram) and y (lower diagram) components of the primary radiation force in the channel. The black contours represent lines where the absolute force is 10% of its maximum value. Figure 2(b) shows the normalized displacement amplitude in a yz cross-section (along the channel) when the source is actuated at 6.851 MHz. The blow-up shows the z (upper diagram) and y (lower diagram) components of the force field in the channel. The normalization is different in figures 2(a) and (b).

diagram) components of the normalized force field in the channel (from which the dashed lines emanate) at 1.97 MHz. The figure is to scale, and hence the channel itself is hard to resolve with the naked eye. Comprehensive frequency scans have been carried out (typically $\pm 15\%$ around the nominal transducer frequency), and we note that there are several actuation frequencies for a given angle of incidence that result in near-1D force fields such as the one depicted in figure 2(a) (i.e., with primarily an x component). However, other resonant frequencies within the investigated interval also include a significant y component of the field that would either levitate or sink particles in the channel (simultaneously with the particle focusing in the x -direction). This predicted phenomenon is experimentally verified and further discussed in section 4.2.2. We note that in no cases do we get a displacement field that could be explained by a simple model such as plane-wave propagation in the wedge and refraction according to Snell's law at surfaces. The reason is that the sizes of all of the involved structures are of the same order of magnitude as the acoustic wavelength λ . In the case of the silicon spacer, our simulations show that the layer is so thin that the field leaks through it in an evanescent fashion.

Figure 2(b) shows the displacement amplitude in a yz cross-section (the vertical plane along the channel, illustrated by a dashed gray line in figure 1(d)) when the Y transducer (cf figures 1(a) and (d)) is actuated at 6.851 MHz. The blow-up inset shows the z (upper diagram) and y (lower diagram) components of the resulting normalized force field in the channel. Above the microchannel, the top glass plate of the chip is designed to function as a reflection layer close to this frequency, and we note that we get a distinct resonant behavior in the y -direction in the glass. More interestingly, a periodic variation in the z -direction both in displacement (in the solid structure) and y component of the force (in the fluid) is predicted at the simulated frequency in figure 2(b). In fact, a similar striated pattern is predicted for all of the found resonance frequencies within the simulated interval (~ 6.85 MHz $\pm 15\%$). Such phenomena are associated with acoustic cavities having large lateral dimensions compared to the axial dimension and to the wavelength, and have previously been observed by, e.g., Townsend *et al* [16].

When comparing the full system resonances in figures 2(a) and (b), we note an interesting difference. In

figure 2(a), the resonance is distributed throughout the full transducer–chip system. In particular, much energy seems to be stored in the wedge, where a complex resonant pattern is observed. On the other hand, we do not find a similar behavior in figure 2(b). Here, most of the energy stored in the solid structures seems to be confined within the glass layers above and below the fluid channel, and not in the wedge. We believe that the reason is the near-1D character of the resonance in figure 2(b), where the glass layer thicknesses are selected as odd multiples of $\lambda/4$. Although we have included air pockets in the silicon layer at $5 \times \lambda/4$ distances from the fluid channel (cf figure 1(a)), we do not obtain a similar simple near-1D resonance in figure 2(a). Instead, we note 'local resonances' below these air pockets (hardly resolved in figure 2(a)). A general explanation for the resonance distribution in both figures is that the glass layers are the primary hosts for the resonance in the solid structure. For all actuation frequencies (~ 2 – 7 MHz), the silicon layer is thin compared to the wavelength ($< 0.1 \times \lambda$) and does not influence the full system resonance to any noticeable extent. One method to improve the chip design in the future is to match the width of the full glass–silicon–glass stack (and not only the channel and silicon widths) with the wavelength.

4.1.2. Impedance spectroscopy. The dependence of the wedge angle and actuation frequency on the coupled transducer–chip resonance was experimentally characterized by impedance spectroscopy. Here, the X transducers with 2.04-MHz PZT elements were chosen for wedge angle optimization. The PZT elements used in these experiments were all circular with a diameter of 10 mm. Figure 3(a) shows the conductances measured over a transducer mounted on a chip with water-filled channel as a function of wedge angle (ranging from 0° to 50°) and frequency (between 1.7 MHz and 2.3 MHz). We note that the strongest resonance peaks are found for the wedge angles 0° and 30° , where the 30° -resonance is close to the nominal resonance frequency of the transducer (2.03 MHz) while the 0° -resonance frequency is shifted to 1.97 MHz. Figures 3(b) and (c) show a more detailed investigation of the 30° -transducer, where the free (unattached) transducer is compared with the transducer mounted on a chip with either a water-filled or an empty (air-filled) channel. As

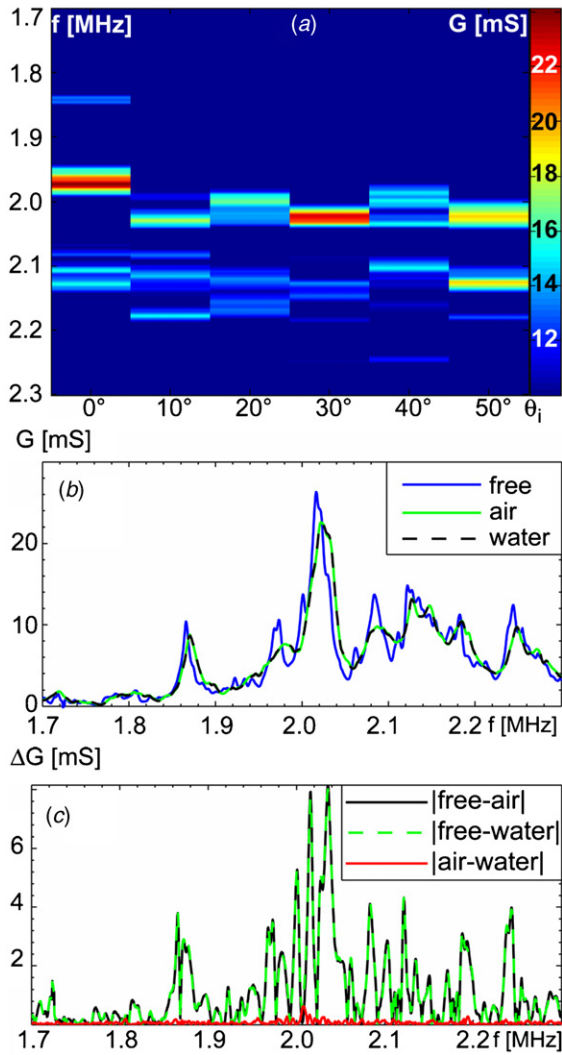


Figure 3. Impedance spectroscopy of the transducer–chip system. Figure 3(a) shows the conductances of five transducers of different wedge angles as functions of the frequency. All values below 10 mS have been cut for clarity. Figure 3(b) shows the conductance of the unattached 30° -transducer in air (‘free’), the transducer mounted on a chip with air-filled channel (‘air’) and on a chip with water-filled channel (‘water’). Figure 3(c) shows the differences between the curves in figure 3(b).

illustrated in figure 3(c) (which plots the differences between the conductances in figure 3(b)), the dependence of the channel medium on the resonance of the transducer–chip system is negligible. This is in contrast to conventional 1D layered resonators, where the fluid layer has a clear dependence on the system resonance [25].

In summary, by choosing an angled wedge transducer we significantly lower the coupling between the channel resonance and transducer resonance. Thus, our simplified design criterion ($L = m\lambda/2$) defined in section 3 is adequate for angled wedges, as opposed to a 1D layered resonator with a plane-parallel coupling layer. Furthermore, we may position the transducer close to an edge of the chip, which is a great advantage for the compatibility of our device with high-performance optical microscopy.

4.1.3. Experimental manipulation performance. In this section, we investigate the dependence of the wedge angle (0° – 50°) and actuation frequency (1.8–2.1 MHz) on the particle manipulation performance in the x -direction, using the same X transducers as in section 4.1.2. The manipulation performance is quantified by an image-analysis-based figure of merit (FOM), which is a measure of the average (along the channel) particle concentration into the vicinity of the pressure node after 15 s of particle focusing (in the x -direction, cf figure 1(b)), relative to the concentration outside the node. Note that the FOM by its definition below is related to the half-wavelength resonance condition, but could easily be adjusted to accommodate another desired pattern.

Each measurement was performed by seeding the channel with a homogenous distribution of $5\ \mu\text{m}$ polyamide beads at a high concentration, stopping the flow, switching on the transducer for 15 s at a low voltage (3 V peak-to-peak) and acquiring a micrograph. Figure 4(a) shows a typical example of such a micrograph where the areas used for calculating the FOM are indicated with colored lines. The yellow lines show the boundaries of the channel as found by automated image analysis (edge detection), and the green lines show the mid-15% of the channel, where the beads end up if the manipulation performance is good. Since the dark regions are beads, we define the FOM as the mean pixel value outside the middle strip divided by the mean pixel value inside the middle strip (after adjusting all images to the same brightness range). Thus, a high FOM corresponds to a high local bead concentration in the center of the channel.

Figure 4(b) presents the results of these measurements, with all FOMs below 1.65 cut out for clarity. Most important, we only obtain a high FOM for the 30° -transducer. Furthermore, we note a clear difference between the manipulation performance shown in figure 4(b) and the impedance spectroscopy results shown in figure 3(a). While impedance spectroscopy predicted the strongest resonances for both the 0° - and 30° -transducers, we note that the 0° -transducer (i.e., with a plane-parallel coupling layer) is not efficient for particle manipulation in the channel. In the impedance measurements, the resonances are typically defined by the solid structure, and do not say anything about the manipulation performance. In order to obtain a high FOM (cf figure 4(b)), the resonances in the solid structure must also create a resonance in the fluid. Therefore, the results in figure 4 are more complex, without any clear interrelation between, e.g., wedge angles.

Finally, we have also investigated the dependence on the transducer position on top of the chip for the 0° - and 30° -transducers, respectively. Two different positions were investigated: close to a chip edge (the same position as used in figure 4(b) and in the simulation in figure 2(a)), and close to the chip center (directly above the channel). Although we could not perform comparative image analysis in the latter case (due to the broken optical path caused by the transducer placed over the channel), manual inspection indicated a similar or slightly lower manipulation performance if the transducers were placed directly above the channel compared to close to an edge. A related conclusion is presented by Neild *et al* [26],

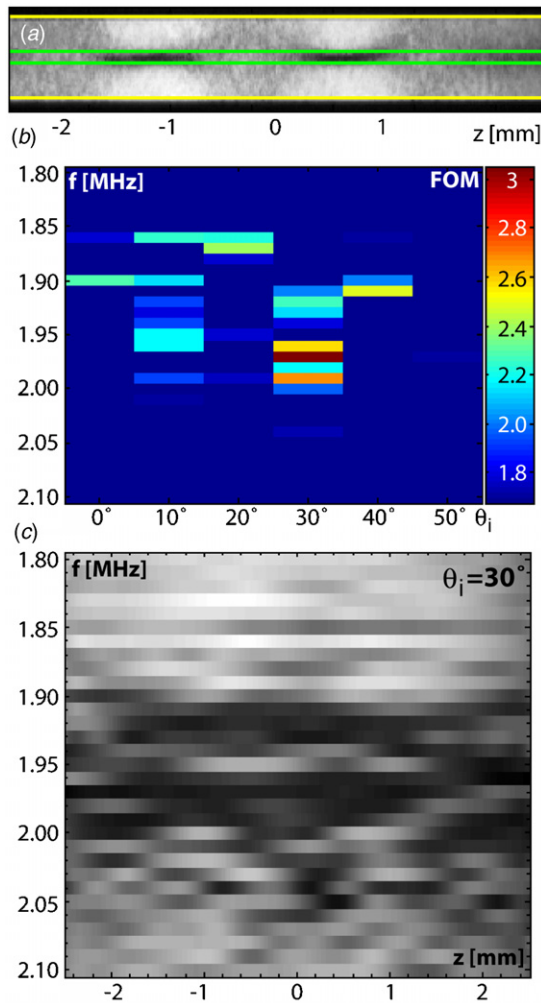


Figure 4. Experimental manipulation performance for different wedge transducer angles and frequencies. Figure 4(a) shows a typical micrograph of manipulated beads in the channel. The colored lines illustrate the areas of interest for the figure-of-merit (FOM) calculation used for quantifying the manipulation performance. Yellow lines indicate the channel walls, and green lines indicate the mid-15% of the channel. In figure 4(b), the FOM is presented for transducer angles ranging from 0° to 50° and frequencies from 1.8 to 2.1 MHz. Values below 1.65 have been cut for clarity. Figure 4(c) shows the local (i.e., not z -averaged) normalized FOM for the 30° -transducer as a function of the position along the channel (z -direction) and of frequency. Thus, figure 3(c) quantifies the periodicity in the FOM at certain frequencies.

who used asymmetric excitation via a strip electrode close to the edge of the piezoelectric element.

It should be noted, however, that our definition of the FOM used in figure 4(b) only gives an estimate of the average manipulation performance in the area photographed. As can be seen both experimentally in figure 4(a) and theoretically in figure 2(b), the performance often varies with location along the channel. Thus, a possible source of error in our quantification of the manipulation performance is if such periodic variations are present but with a period larger than the area photographed. Figure 4(c) shows a characterization of the manipulation performance along the channel for the transducer with the highest FOM (with the 30° -wedge).

We note that at the frequency giving the highest FOM (1.97 MHz) the particle focusing along the channel is fairly uniform, but also that a periodic pattern such as at 2.00 MHz (cf figure 4(c)) can result in a FOM above the cut at 1.65 in figure 4(b). Such a periodic manipulation performance phenomenon is often negligible and invisible when the chip is operated in a flow-through mode. On the other hand, if the flow in the channel is very low or under no-flow conditions, such effects become very important. We demonstrate an application of a periodic resonance in section 4.2.1 (2D arraying).

4.2. Verification of design

4.2.1. Single-frequency and no-flow operation: 2D arraying.

Figure 5 illustrates commonly observed distributions of manipulated beads in a microchannel for different frequencies close to the nominal X transducer frequency (~ 2 MHz, aimed for focusing in the x -direction, cf figure 1(b)), and compares the experimental distributions (micrographs) with modeled force fields. The simulation graphs (below each micrograph in figure 5) are selected areas from numerical modeling in two dimensions (xz plane, a ‘top view’) of the entire chip, which means that the comparison is semi-quantitative (in terms of, e.g., absolute frequency matching) [15]. The ‘straight’ node shown in figure 5(a) is actually less common than the ‘wobbly’ node (figure 5(b)) or the ‘periodic’ node (figure 5(c)). This fact is reflected in previous observations of similar node shapes in microchips (e.g., in [10, 16, 19, 26]). As seen in the modeling results in figures 5(b), (c), the ‘wobbly’ or ‘periodic’ shapes are predicted in theory if the resonance of the whole transducer–chip system is taken into account. Thus, the phenomenon is typically associated with ultrasonic manipulation in microfluidic chips, where the microchannel serves as a closed cavity of very small volume relative the whole chip volume. The result is complex 3D enclosure modes of the solid structure, which are coupled with the microchannel resonance. It should be noted, however, that in flow-through applications, e.g., continuous particle separation [4], the effects of ‘wobbly’ or periodic’ nodes are often averaged out and therefore not even visible. Still, the effects must be considered in no-flow applications as discussed here. Finally, it should also be noted that while the model can predict the shape of the observed force field distributions, it is very difficult to predict the corresponding actuation frequency with high accuracy. One reason is the uncertainty in the sound speed in the modeled materials.

We will now demonstrate an example of the use of the ‘wobbly’ and ‘periodic’ effects in single-frequency fields in microchannels. Figures 6(a) and (b) illustrate a selected area of the full simulated field at 3.98 MHz (i.e., a full-wavelength resonance across the x -direction of the channel), where the actuation frequency is chosen in order to achieve x (figures 6(a)) and z (figure 6(b)) force components in the channel of similar magnitudes. Figure 6(c) displays predicted trapping sites (dark spots), based on the intersections between the predicted potential wells of each force component x and z in figures 6(a), (b), respectively. For this purpose, we have

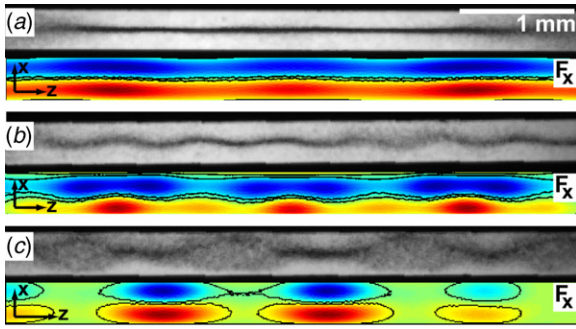


Figure 5. Comparison between experimental manipulation performance (micrographs) and modeled normalized forces (x components only, red is positive and blue negative) in three characteristic cases: the ‘straight’ node (a), the ‘wobbly’ node (b) and the ‘periodic’ node (c). The contour lines correspond to the absolute forces being equal to 10% of the maximum value. The normalization is different in the three simulations. The scalebar in (a) applies to all images. The micrographs are acquired from the frequency scans discussed in section 4.1.3. The frequencies used in the micrographs were (a) 1.88 MHz, (b) 1.98 MHz and (c) 2.03 MHz, and in the simulations (a) 1.86 MHz, (b) 1.92 MHz and (c) 1.87 MHz.

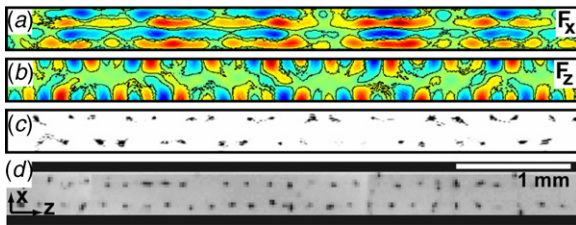


Figure 6. Two-dimensional (2D) arraying of particles in a straight channel. Figures 6(a) and (b) show modeling of the x and z components, respectively, of the force during single-frequency actuation (at 3.98 MHz). The contour lines are forces 10% of the maximum value. Figure 6(c) illustrates the results of calculations on probable trapping sites based on the results shown in figures 6(a) and (b). Figure 6(d) demonstrates a corresponding experiment, where 2.8 μm beads are arranged in a 2D array of small bead aggregates at 4.00 MHz actuation.

defined a point \mathbf{r}_{well} to be in the potential wells in figures 6(a) and (b) by the condition that

$$|\mathbf{F}_{\text{PR}}(\mathbf{r}_{\text{well}})| < 0.1 \cdot |\mathbf{F}_{\text{PR}}|_{\text{max}} \quad \text{and} \quad (6)$$

$$\nabla F_{\text{PR},i}(\mathbf{r}_{\text{well}}) < -0.02 \cdot |\nabla F_{\text{PR},i}|_{\text{max}},$$

where the symbol $||_{\text{max}}$ means the maximum of the absolute value, and the second condition must hold for the gradient of both components of \mathbf{F}_{PR} , i.e., $i = x$ and $i = y$.

Thus, simulation predicts that it is possible to arrange particles in a 2D array of small aggregates by single-frequency actuation of a simple straight microchannel. The prediction is experimentally confirmed in figure 6(d), where 2.8 μm fluorescent polystyrene beads were actuated for 5 min at 4.00 MHz and 8 V_{pp} by a 48°-wedge Z transducer¹. Interestingly, both theory and experiments indicate an irregular and complex force distribution resulting in, e.g., ‘missing’ nodes, ‘out-of-place’ (compared to a symmetric grid) nodes

¹ The result that the 30°-wedge transducer is optimal is valid when the target application was uniform focusing, which is not the case here.

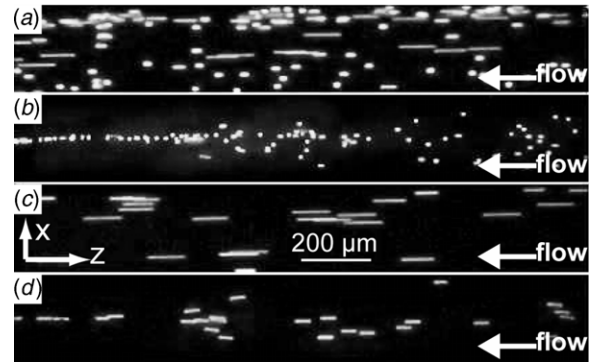


Figure 7. Two-dimensional (2D) alignment of 10.8 μm beads in flow-through operation using two independent transducers. Figure 7(a) shows the distribution of beads in the channel without any acoustic fields. Figure 7(b) shows the effect of focusing of beads towards a vertical plane in the middle of the channel. Figure 7(c) shows the effect of levitation of beads towards a horizontal plane near the middle of the channel. Both figures 7(b) and (c) are 1D manipulation functions corresponding to the modeled force fields in figures 2(a) and (b), respectively. Figure 7(d) shows 2D alignment of the beads into the centerline of the channel by dual-frequency actuation. This is a combination of the focusing and levitation functions in figures 7(b) and (c).

and elongated shape of some nodes (cf figures 6(c) and (d)). This is a typical effect of strong mode coupling in orthogonal directions during single-frequency actuation.

4.2.2. Dual-frequency and flow-through operation: 2D alignment. We will now demonstrate an important flow-through application of two different-frequency, uncoupled, near-1D, orthogonal fields used for 2D particle alignment. Figure 7 shows images acquired with 19 ms exposure time, demonstrating 1D focusing (figure 7(b)), 1D levitation (figure 7(c)) and 2D alignment (figure 7(d)) of fluorescent 10.4 μm beads pumped through the channel at 5 $\mu\text{l s}^{-1}$, and compared with the initial no-field operation (figure 7(a)). In the experiment, the system is excited at either 1.97 MHz/5.0 V_{pp} by a 30°-wedge X transducer (figures 7(b) and (d)), and/or at 6.90 MHz/5.0 V_{pp} by a 20°-wedge Y transducer (figures 7(c) and (d)). Thus, focusing (figure 7(b)) and levitation (figure 7(c)) are single-frequency manipulation functions, while alignment (figure 7(d)) is a dual-frequency manipulation function.

Without any ultrasonic actuation (cf figure 7(a)), a typical and general microfluidic effect is a wide distribution in speeds of the beads due to the wide distribution of beads in the cross-section (in both x - and y -directions) in combination with the laminar flow and no-slip boundary conditions of the medium. In particular, beads that settle by gravity to the bottom surface of the microchannel are partly retained (‘stuck’) by the surface interaction, resulting in very low and irregular, or no speed. The latter effect is still present in figure 7(b), where a significant majority of the focused particles move close to the bottom surface at low speed. In fact, we believe that the difference in the relative amount of beads close to the bottom surface in figures 7(a) and (b) is caused by the pseudo-1D resonance in the x -direction, having

a small but not negligible (negative) y component pushing the beads towards the bottom of the channel. Such lateral components are predicted in theory (e.g., the inset in figure 2(a) shows a positive y component, but simulations at other nearby frequencies confirm the existence of negative y components).

Streak length measurements of the imaged beads in figure 7 can be used for the quantification of the bead speed distribution. For example, our measurements demonstrate that the standard deviation of the speeds is lowered by more than a factor of 2 if the levitation function (figure 7(c)) is compared with no-field operation (figure 7(a)). Finally, figure 7(d) shows alignment of the beads into the centerline of the channel by actuating both transducers simultaneously. The beads are now centered both vertically (levitated) and horizontally (focused), i.e., aligned and centered in two dimensions in the channel with trajectories parallel to the channel walls. In agreement with the observation made for the focusing function (figure 7(b)), we also note that the actual bead speeds in figure 7(d) are lower than in figure 7(c). A reasonable explanation is that the vertical position of beads is primarily defined by the equilibrium between the lateral (negative, y -directed) component of the focusing (x -directed) field and the (positive, y -directed) levitating field. Furthermore, the standard deviation of the velocity distribution is now almost negligible, since all beads follow the same fluid streamline. Thus, figure 7(d) shows that with our system it is possible to guide suspended particles or cells through a microfluidic channel at constant speed and constant cross-sectional position, without any contact with the channel walls. Direct benefits are reduced sample loss or contamination, a retained spatial confinement of particles along the channel in an injected sample volume, and improved compatibility with high-resolution microscopy-based optical monitoring of particles and cells (by matching the optical focal plane with the levitation plane).

5. Summary and conclusion

Analysis of the coupling method with wedge transducers clearly shows that it is advantageous to use an angled wedge compared to a simple plane-parallel coupling layer (referred to as a 0° -wedge in section 4). In our coupling analysis for the focusing manipulation function, we conclude that the X transducer with a 30° -wedge is the optimal choice. It is also noted that the optimal position of the 30° -wedge transducer is close to a chip edge, and not directly above the channel (close to the chip center). Such asymmetric transducer placement is not only advantageous for the coupling, but also fully compatible with trans-illumination-based high-resolution optical microscopy. A future design improvement is to match not only the height, but also the width of the whole chip (including all three layers) with the wavelength.

Concerning the manipulation characteristics, we note that one-dimensional (1D) resonances excited at single frequencies do not exist in microchannels or microchips. Any resonance ranges from a complex 3D resonance with strong coupling effects, to a pseudo-1D resonance with only minor lateral force components, or variations in the axial component

along the lateral direction. Typical effects of pseudo-1D resonances in a fluid channel are ‘wobbly’ and ‘periodic’ nodes (cf figure 5). Under certain circumstances the forces parallel and perpendicular to the channel are of equal magnitudes, which can give rise to an array of isolated trapping sites (cf figure 6). This is one strategy to obtain a 2D manipulation function by single-frequency actuation. Another strategy is to superpose pseudo-1D resonances by dual-frequency actuation (cf figure 7). While strong coupling effects have been observed and theoretically predicted in the case of two frequencies of very small difference [17], we have not observed any coupling effects in our measurements performed at two frequencies of larger difference (cf figure 7). A general multi-frequency strategy to minimize coupling effects is to avoid frequencies that are close to multiples of each other.

In the future, our device can be used for high-resolution optical monitoring of 2D aligned particles or cells, or of cells positioned in an array of small aggregates for long-term, dynamic optical characterization.

Acknowledgments

This paper was generated in the context of the *CellPROM* project, funded under the 6th Framework Program of the European Community (Contract No NMP4-CT-2004-500039). The work was also supported by the Swedish Research Council for Engineering Sciences.

References

- [1] Hawkes J J, Barber R W, Emerson D R and Coakley W T 2004 Continuous cell washing and mixing driven by an ultrasound standing wave within a microfluidic channel *Lab Chip* **4** 446–52
- [2] Petersson F, Nilsson A, Jönsson H and Laurell T 2005 Carrier medium exchange through ultrasonic particle switching in microfluidic channels *Anal. Chem.* **77** 1216–21
- [3] Harris N R, Hill M, Beeby S, Shen Y, White N M, Hawkes J J and Coakley W T 2003 A silicon microfluidic ultrasonic separator *Sensors Actuators B* **95** 425–34
- [4] Petersson F, Nilsson H, Holm C, Jönsson H and Laurell T 2004 Separation of lipids from blood utilizing ultrasonic standing waves in microfluidic channels *Analyst* **129** 938–43
- [5] Haake A, Neild A, Radziwill G and Dual J 2005 Positioning, displacement, and localization of cells using ultrasonic forces *Biotech. Bioeng.* **92** 8–14
- [6] Bazou D, Foster G A, Ralphs J R and Coakley W T 2005 Molecular adhesion development in a neural cell monolayer forming in an ultrasound trap *Mol. Membr. Biol.* **22** 229–40
- [7] Hultström J, Manneberg O, Dopf K, Hertz H M, Brismar H and Wiklund M 2007 Proliferation and viability of adherent cells manipulated by standing-wave ultrasound in a microfluidic chip *Ultrasound Med. Biol.* **33** 175–81
- [8] Wiklund M, Toivonen J, Tirri M, Hänninen P and Hertz H M 2004 Ultrasonic enrichment of microspheres for ultrasensitive biomedical analysis in confocal laser-scanning fluorescence detection *J. Appl. Phys.* **96** 1242–48
- [9] Lilliehorn T, Nilsson M, Simu U, Johansson S, Almqvist M, Nilsson J and Laurell T 2005 Dynamic arraying of microbeads for bioassays in microfluidic channels *Sensors Actuators B* **106** 851–8

- [10] Wiklund M, Günther C, Jäger M, Fuhr G and Hertz H M 2006 Ultrasonic standing wave manipulation technology integrated into a dielectrophoretic chip *Lab Chip* **6** 1537–44
- [11] Laurell T, Petersson F and Nilsson A 2007 Chip integrated strategies for acoustic separation and manipulation of cells and particles *Chem. Soc. Rev.* **36** 492–506
- [12] Neild A, Oberti S, Beyeler F, Dual J and Nelson B J 2006 A micro-particle positioning technique combining an ultrasonic manipulator and a microgripper *J. Micromech. Microeng.* **16** 1562–70
- [13] Manneberg O, Hultström J, Hertz H M, Brismar H and Wiklund M 2006 Elementary manipulation functions for gentle and long-term handling of cells in microchannels by ultrasonic standing waves *Proc. 10th Ann. Eur. Conf. on Micro & Nanoscale Technologies for the Biosciences (NanoTech Montreux, Switzerland)*
- [14] Evander M, Johansson L, Lilliehorn T, Piskur J, Lindvall M, Johansson S, Almqvist M, Laurell T and Nilsson J 2007 Noninvasive acoustic cell trapping in a microfluidic perfusion system for online bioassays *Anal. Chem.* **79** 2984–91
- [15] Hagsäter S M, Glasdam Jensen T, Bruus H and Kutter J P 2007 Acoustic resonances in microfluidic chips: full-image micro-PIV experiments and numerical simulations *Lab Chip* **7** 1336–44
- [16] Townsend R J, Hill M, Harris N R and White N M 2006 Investigation of two-dimensional acoustic resonant modes in a particle separator *Ultrasonics* **44** e467–71
- [17] Oberti S, Neild A and Dual J 2007 Manipulation of micrometer sized particles within a micromachined fluidic device to form two-dimensional patterns using ultrasound *J. Acoust. Soc. Am.* **121** 778–85
- [18] Svennebring J, Manneberg O and Wiklund M 2007 Temperature regulation during ultrasonic manipulation for long-term cell handling in a microfluidic chip *J. Micromech. Microeng.* **17** 2469–74
- [19] Manneberg O, Hagsäter S M, Svennebring J, Hertz H M, Kutter J P, Bruus H and Wiklund M 2008 Spatial confinement of ultrasonic forces in microfluidic channels *Ultrasonics* at press (doi:10.1016/j.ultras.2008.06.012)
- [20] Gor'kov L P 1962 On the forces acting on a small particle in an acoustic field in an ideal fluid *Sov. Phys.—Dokl.* **6** 773–75
- [21] Gröschl M 1998 Ultrasonic separation of suspended particles: I. Fundamentals *Acta Acust.* **84** 432–47
- [22] Wiklund M and Hertz H M 2006 Ultrasonic enhancement of bead-based bioaffinity assays *Lab Chip* **6** 1279–92
- [23] <http://www.comsol.com/products/multiphysics/>
- [24] <http://www.mathworks.com>
- [25] Hill M, Shen Y and Hawkes J J 2002 Modelling of layered resonators for ultrasonic separation *Ultrasonics* **40** 385–92
- [26] Neild A, Oberti S and Dual J 2007 Design, modeling and characterization of microfluidic devices for ultrasonic manipulation *Sensors Actuators B* **121** 452–61